Magn Reson Imaging. Author manuscript; available in PMC 2013 November 28.

Published in final edited form as:

Magn Reson Imaging. 2012 December ; 30(10): 1416–1423. doi:10.1016/j.mri.2012.04.011.

Imaging of stroke: a comparison between X-ray fluorescence and magnetic resonance imaging methods

Weili Zheng[a], **E. Mark Haacke**[a], **Samuel M. Webb**[b], and **Helen Nichol**[c,*]

[a]HUH-MR Research/Radiology, Wayne State University, Detroit, MI, USA

[b]Stanford Synchrotron Radiation Lightsource, CA, USA

[c]Department of Anatomy & Cell Biology, University of Saskatchewan, 107 Wiggins Rd., Saskatoon, SK, Canada S7N5E5

Abstract

A dual imaging approach, combining magnetic resonance imaging to localize lesions and synchrotron rapid scanning X-ray fluorescence (XRF) mapping to localize and quantify calcium, iron and zinc was used to examine one case of recent stroke with hemorrhage and two cases of ischemia 3 and 7 years before death with the latter showing superficial necrosis. In hemorrhagic lesions, more Fe is found accompanied with less Zn. In chronic ischemic lesions, Fe, Zn and Ca are lower indicating that these elements are removed as the normal tissue dies and scar tissue forms. Both susceptibility and T2* maps were calculated to visualize iron in hemorrhages and validated by XRF Ca and Fe maps. The former was superior for imaging iron in hemorrhagic transformation and necrosis but did not capture ischemic lesions. In contrast, T2* could not differentiate Ca from Fe in necrotic tissue but did capture ischemic lesions, complementing the susceptibility mapping. The spatial localization, accurate quantitative data and elemental differentiation shown here could also be valuable for imaging other brain tissue damage with abnormal Ca and Fe content.

Keywords

Susceptibility mapping; Synchrotron X-ray fluorescence; Hemorrhage; Stroke; Iron; Calcium

1. Introduction

While iron is known to play an important role in hemorrhagic stroke, the role of other elements has been largely neglected. The elemental changes associated with chronic ischemic lesions are largely unknown, but when they form magnetic minerals (paramagnetic ferritin or hemosiderin or diamagnetic calcifications), they may contribute to signal changes in MR images. Synchrotron rapid scanning X-ray fluorescence (SRS-XRF) mapping simultaneously localizes and accurately quantifies multiple metals in tissue slices or small whole organisms [1–4]. This well-established, element-specific analytical technique has been applied to map slices of human brain, using newer high-resolution SRS-XRF [5–8].

*Corresponding author: Fax: +1 306 966 4298. h.nichol@usask.ca (H. Nichol).

Recently, some of these results have been compared with magnetic resonance imaging (MRI) scanning [9–11].

SRS-XRF imaging has not previously been applied to study human stroke or animal models of stroke [12]. Much of our fundamental understanding of the pathophysiology of ischemic and hemorrhagic stroke has arisen from work on a variety of animal models using behavioral, cell biology and molecular biology techniques [13]. None of the animal models fully replicates human stroke and studies in animals tend to be short-term. In the cases shown here, the strokes were not immediately fatal and occurred years or weeks before death. One of the aims of this work is to determine the feasibility of comparing the measurement of iron content obtained from SRS-XRF with that obtained from MRI using quantitative susceptibility mapping and T2* mapping.

Iron has clinical importance [14,15], not only because it is required for normal brain function [7] but also because the chemical reactivity of free iron likely contributes to brain damage by leading to the formation of free radicals [14]. It also serves as an important endogenous marker of blood products in T2* weighted gradient echo (GRE) MR that is commonly used to image stroke *in vivo* [16,17]. Susceptibility weighted imaging (SWI) based on GRE is the most sensitive MR method both for non-heme iron [14,18–20] and heme iron [21–25]. Hemorrhage, whether primary or secondary to ischemia undergoes a transformation from deoxy-hemoglobin to methemoglobin and later hemosiderin [26]. Each of these sources of iron has different T1 and T2* properties [27]. SWI is sensitive to iron in all three forms [21]. Thus, in suspected acute stroke, SWI serves as a key sequence in detecting hemorrhage within the region of infarction. However, SWI data are known to have a blooming effect that magnifies the hemorrhagic lesions [in GRE with long echo time (TE)], and the phase image is dependent on field strength, echo time, the object's relative orientation to the main field and its geometric shape [28–38]. Since susceptibility maps reconstructed from SWI phase images and T2* maps reconstructed from multi-echo SWI magnitude images are free from the above concerns, they are the most promising way to depict and quantify iron in hemorrhagic lesions [32,34–37,39,40].

In this study, we aim to determine whether SWI, susceptibility maps or T2* correlate best with elemental mapping of iron (Fe) and calcium (Ca) using SRS-XRF. Based on the known effects outlined above, we hypothesize that susceptibility maps will provide the best spatial correlation of both Fe and Ca found in hemorrhagic and chronic stroke lesions.

2. Methods

2.1. Study samples and analysis procedures

Frozen coronal sections of human cadaveric brains were obtained from the Human Brain and Spinal Fluid Resource Center (HSB), Los Angeles, CA, under the University of Saskatchewan ethics approval BioREB 06–250. The known clinical features of the cases are summarized in Table 1. To reduce storage artifacts such as leaching of metals, the frozen slices were fixed in buffered formalin for 6 hours, drained and sealed in plastic immediately prior to initial synchrotron imaging of the surface of the slice.

Thick brain slices (56~64 mm wide×52~84 mm long and 10 mm thick) were first embedded in 5% gelatin for MR imaging to identify the internal hemorrhagic lesions. Second, internal regions-of-interest (ROI), identified by MRI, were exposed by slicing the original slices into thinner sections (1–3 mm thick), parallel to the surface. To preserve the elements, these thinner slices were immediately sealed under polypropylene without any rinsing or other treatments. Third, SRS-XRF mapping was done at the Stanford Synchrotron Radiation Lightsource (SSRL) on beamline 10–2. In all cases, the XRF maps were co-registered with the MRI images at the same ROI. Fourth, the tissue in ROI was embedded in paraffin for histology following conventional procedures.

2.2. MRI imaging parameters

MR images were collected on a 3T Siemens VERIO system using a 12-channel receive head-matrix coil. Phase and magnitude images were collected using T2* weighted multi-echo SWI sequence with 11 echoes (TR=40 ms, FA=15°). The images were acquired with a resolution of 0.5 mm × 0.5 mm in the phase and readout directions and 0.7 mm in the slice direction (coronal) with a bandwidth of 465 Hz/pixel, a field-of-view of 256×192 mm, a 512×384 matrix with 40 slices. The first echo time was 5.74 ms with the subsequent 10 echoes being spaced 2.48 ms apart. For the multichannel coil data, an adaptive phase combination was used. The susceptibility maps were reconstructed from the second echo phase images (TE=8.22 ms). A high-pass filter of 64×64 was first used to remove the background field, then the SWIM algorithm discussed in Haacke et al. [29] was applied to generate the susceptibility map. All the procedures were done using SPIN (Signal Processing in NMR, Detroit, MI, USA) software. T2* maps were calculated from multi-echo SWI images in SPIN. Fluid Attenuated Inversion Recovery (FLAIR) images were collected in the coronal direction with TR=9000 ms, TE=74 ms, TI=2500 ms, 1×1×1-mm resolution, an in-plane matrix size of 256×192 with 32 slices.

2.3. Synchrotron rapid scanning X-ray fluorescence mapping parameters

The samples were mounted vertically, at 45° to the incident beam and raster-scanned using a set of motorized stages. The incident beam (12 keV) passing through a tantalum aperture produced a 100 μm×100 μm spot on the sample. Beam exposure was 25 or 35 ms per 100-μm pixel. Fluorescent energy windows were centered for Fe (6.21–6.70 keV), Ca (3.52–3.96 keV), and Zn (8.38–8,98 keV) as well as other biologically interesting elements such as Mn (5.69–6.09 keV) and Cu (7.85–8.25 keV). Fluorescence was normalized against incident X-ray beam intensity. Elements were quantified by comparison of signal strength with XRF calibration standards (Micromatter, Vancouver, BC, Canada) following the procedure described by Hopp et al. [9] using the Microanalysis Toolkit (http://ssrl.slac.stanford.edu/~swebb/smak.html).

The escape depth of fluorescence from the sample increases with energy of the fluorescent X-ray, and thus, for the K-edge emission lines, increases with the atomic number of the element being mapped. Fluorescence arising from low Z elements (such as sulfur) was completely blocked by the polypropylene film under which the brain tissue was sealed. We were able to measure some calcium signal through the polypropylene film but an uncovered, flat and dry surface would be needed for an accurate quantification. Therefore, only areas

with high calcium are described with respect to surrounding tissue (marked with white arrows in the figures) but not quantified in Table 2.

2.4. Histology of sections

Upon completion of elemental mapping, portions of the brain that were of interest were excised and placed in a tissue processor for standard paraffin embedding. Briefly, tissue is dehydrated in progressively more concentrated ethanol followed by xylene and then molten paraffin wax. In all cases, paraffin-embedded tissue was sectioned from the surface that had been previously mapped using SRS-XRF and stained with hematoxylin and eosin for routine examination and Luxol fast blue to resolve demyelinated regions.

3. Results

3.1. XRF findings

Visual inspection of the thin (1–3 mm thick) brain slices showed regions of discoloration and histology revealed extensive tissue damage in these areas (Fig. 1). In the XRF maps, the apparent increase in elements around the edge is likely due to the summation of counts arising from both the surface and the edge of these thick slices (i.e., an edge effect) rather than from the deposition of elements from the formalin solution [41]. ROIs of hemorrhage, white matter (WM), gray matter (GM) and ischemic WM infarct for Table 2 are outlined in the gray-scaled Fe map (Fig. 1, row 5). Regions of interest for hemorrhage were defined by manually drawing some of the lesions on the XRF Fe maps. ROIs of normal WM and GM were identified in FLAIR images [42] and manually drawn on the XRF maps. Ischemic infarcts were seen in the FLAIR images as hyper-intense areas [42]. Therefore, ROIs for WM infarct measurements were chosen from the FLAIR images by using thresholding (i.e., keeping signals within the interval 600<intensity<1200) inside the boundary drawn to cover the infarct (using SPIN). These regions were carefully drawn to exclude gelatin, hemorrhage, and cortex. The thresholded regions were then coregistered to the XRF maps.

The first autopsy case represents a stroke 10 days before death. The regions with visual discoloration were rich in iron (Fig. 1, red arrows in first column). The concentrations of Fe and Zn in lesions and in normal tissues for all the cases shown in Fig. 1 are summarized in Table 2. The amount of an element in lesions was compared with normal white matter in Table 2. Less iron ($P<.05$, Table 2) was seen in the chronic ischemic WM infarct. Zinc was abundant in the undamaged cortical U fibers and was significantly reduced in the chronic ischemic WM infarct ($P<.05$, Table 2) and hemorrhagic lesions ($P<.05$, Table 2). The calcium seen around and along the right edge of the brain appeared to be an edge effect, whereas substantially high calcium (estimated at >100 μg Ca/g wet weight, white arrow in the first column) along the left side of the brain was associated with hemorrhage. The calcium in this area (white arrow in the first column) was not colocalized with iron or zinc.

The second and third autopsy cases represent chronic ischemic lesions (Fig. 1, red arrow in the second and third columns) associated with tissue necrosis or hemorrhagic transformation that could have occurred years before death. Visual inspection of the brain slices showed regions of discoloration associated with the necrotic tissue and hemorrhages. There was no

hematoma in either case but there was extensive tissue damage, demyelination and glial scarring.

In the second case, the regions rich in iron (red arrow in the second column) contained smaller accumulations of zinc, and calcium (Fig. 1, second column) and calcium colocalized with zinc (white arrows). Depletion of iron ($P<.05$, Table 2) was seen in the ischemic lesion. Zinc was significantly reduced in the iron-rich region ($P<.05$, Table 2) and the chronic ischemic WM infarct ($P<.05$, Table 2).

In the third case, zinc and calcium co-localized in one area (upper box in the calcium and zinc maps, third column) without the presence of iron, while in another location (lower box in the calcium and zinc maps, third column) zinc and calcium were found in an iron-rich region. Generally, there was less zinc ($P<.05$, Table 2) in very high-iron areas. Other findings of this case were a central region of ischemic damage (chronic necrosis) that was characterized by less iron and zinc (Table 2).

3.2. Correlation of MRI with XRF

In the recent stroke (case 1), there was excellent correspondence between higher iron in XRF and susceptibility change in the hemorrhage (Fig. 2, red arrows in the first row). These lesions could be visualized in the T2* map but the susceptibility map provided superior spatial localization and contrast of the iron distribution. Outside the hemorrhage, the ischemic lesion was seen as hyper-intense in FLAIR and hyper-intense in the SWI magnitude image at TE=18.5 ms (indicating an increase in T2*), but not seen at TE=8.2 ms (date not shown). In this case, the ischemic lesion could not be differentiated from normal tissue in the susceptibility map.

In the second case, the iron-rich regions (Fig. 1, second column) had little signal left in the SWI data due to very short T2*, making it difficult to make any quantitative comparison with the XRF Fe map. Therefore, the MR data of this case was not shown here.

In the necrotic region of the third case, there was excellent correspondence between iron in XRF and susceptibility mapping as well as T2* (Fig. 2, red arrows in the second row), but the susceptibility map provided superior localization and contrast. In this tissue sample, calcium-rich spots (Fig. 2, white arrows in the second row) probably represented calcifications. These were captured by the susceptibility map, SWI magnitude image and the T2* map but were not differentiated from iron in the SWI magnitude image and T2* map because calcium and iron both cause T2* shortening. In contrast, diamagnetic calcium appeared as a negative signal and paramagnetic iron with a positive signal in the susceptibility map.

4. Discussion

In conventional stroke imaging, signal loss in T2* weighted gradient echo images is interpreted as caused by the dephasing effect from spatially varying local magnetic fields due to iron deposits. However, tissue damage or changes in tissue susceptibility can also cause signal loss. Phase images are sensitive to the geometric shape of a hemorrhagic lesion

and its orientation to the main field. Phase images were not included in the analysis because they did not have as good a correlation to the iron distribution as the magnitude image and the susceptibility map. The advantage of the susceptibility map is that it corrects for the geometry effects present in the phase images and provides a geometry independent solution [28–38]. However, on occasion, the phase is still of interest for visualizing local field variations. Due to the limitation of T2*-weighted gradient echo images and phase images, T2* map and susceptibility map provide more accurate imaging of paramagnetic iron arising from blood products in the hemorrhagic lesions.

Quantifying iron based on an MR susceptibility map required two steps. The first was susceptibility mapping of the phase images. The second was establishing the correlation between iron concentration and the susceptibility change through a reliable spatial registration of the two images. Poor registration hindered the voxel-by-voxel quantitative comparison, which was the major obstacle of this work. Though susceptibility mapping has been used to visualize hemorrhage in stroke patients [34], its ability to quantitatively visualize iron in stroke hemorrhages has not yet been validated. Ex vivo validation of susceptibility mapping of iron particles in rat brain with histology shows accurate localization of iron [32], but this is a qualitative, not a quantitative, validation. XRF Fe mapping presented in this paper provides a possible solution for quantitative validation of susceptibility mapping when the source of susceptibility is known to be predominantly iron. Ideally, if registration error is negligible, there can be a voxel-by-voxel matching of XRF iron maps and susceptibility maps [43] to validate both the spatial localization and the iron concentration. Unfortunately, due to lack of reliable registration landmarks, grey/white matter boundaries, voxel-by-voxel quantitative comparison, as previously reported for multiple sclerosis samples [43], was not achievable for the data in this study. Therefore, the best matching angle between the two images was chosen for comparison. In multiple sclerosis studies [43], samples contained only a few small focal lesions. There was almost no damage to the grey/white matter boundaries in those samples which were important landmarks and were essential for successful registration. In contrast, in the stroke samples, especially those with secondary hemorrhage, the damage was vast. The GM/WM contrast in the XRF images and the susceptibility map was lost as seen in Fig. 2. This prevented us from establishing a voxel-by-voxel quantitative correlation between iron concentration and the susceptibility change.

Our results show that susceptibility mapping localized the hemorrhages more accurately than T2* mapping and this is in agreement with previous studies [44]. Iron and calcium identified with the SRS-XRF were readily visualized by susceptibility mapping from SWI. It is particularly interesting to note that in the old stroke sample (case 3), T2* lost its spatial accuracy in detecting iron-rich lesions but susceptibility mapping did not. There are two possible reasons why this occurs. The old stroke lesion could have lower water content than newer lesions which would cause a decrease of T2 and hence T2* confounding the decrease of T2* due to the presence of iron [45]. Alternatively, the amount of iron present may be too small (in some areas) to cause an observable T2* effect, but the phase is so sensitive to iron that susceptibility mapping is able to differentiate iron laden from normal tissue. T2* is superior to susceptibility mapping to distinguish recent stroke infarcts (more water content than in normal tissue [46], case 1) due to its sensitivity to water content, whereas

susceptibility of infarct and normal tissue is the same. Therefore, combining T2* mapping and susceptibility mapping is a good solution to resolve both ischemia and hemorrhage [44,47].

Although our results indicate a good spatial correspondence between total iron by XRF and susceptibility mapping in both recent and old stroke, iron quantification can still be a problem in differentiating hemorrhages in their various forms such as hemoglobin (diamagnetic), deoxyhemoglobin (paramagnetic), methemoglobin (paramagnetic), hemichromes (diamagnetic), ferritin (paramagnetic) and hemosiderin (paramagnetic) [26] with different susceptibilities [15–17]. Thus, quantification of hematoma iron based on susceptibility values or T2* values becomes unreliable [26,48] in acute stroke until heme iron is metabolized and stored in ferritin or hemosiderin.

The other element that is of interest from the point of view of MRI is calcium. This study indicates that susceptibility mapping should be superior to T2* in visualizing calcifications in a variety of clinical contexts, including calcifications arising in stroke. In very old lesions, calcium was more condensed and associated with zinc. Zinc has been previously identified in brain calcifications in Fahr's disease [49] and recently, elevated calcium and zinc have been seen adjacent to hemorrhages in a rat model of intracerebral hemorrhage [50].

Susceptibility mapping provides a clear separation between calcium and iron since the former has a negative susceptibility relative to white matter and the latter a positive susceptibility relative to white matter. In T2* data, both elements create signal losses that make their source virtually indistinguishable.

5. Conclusion

In this study of cadaver brains, SRS-XRF mapping of iron, zinc and calcium revealed their elemental distributions in stroke. These distributions were then compared to the MR data in order to reveal how well either T2* mapping or susceptibility mapping could identify said regions. We found that hemorrhagic regions had higher Fe, Zn and Ca but that these elements did not always co-localize. We also found that regions of ischemic damage in white matter had lower levels of Fe, Zn and Ca than adjacent tissue. Susceptibility mapping accurately localized iron in hemorrhagic regions and necrotic tissue while T2* localized ischemic lesions better but could not distinguish Fe from Ca. This approach could be applied to image any brain lesion with abnormal Ca and Fe content to enhance our understanding of the pathology post stroke in order to gain a handle on the underlying chemical mechanisms.

Acknowledgments

This work is supported by the Canadian Institutes of Health Research (CIHR)/Heart and Stroke Foundation of Canada (HSFC) Synchrotron Medical Imaging Team Grant #CIF 99472.

Portions of this research were carried out at the Stanford Synchrotron Radiation Lightsource, a Directorate of SLAC National Accelerator Laboratory and an Office of Science User Facility operated for the US Department of Energy Office of Science by Stanford University. The SSRL Structural Molecular Biology Program is supported by the DOE Office of Biological and Environmental Research, and by the National Institutes of Health, National Center for Research Resources, Biomedical Technology Program (P41RR001209).

This work was supported in part by National Institutes of Health Award Number NHLBI R01HL062983. The content is solely the responsibility of the authors and does not necessarily represent the official views of the National Heart, Lung, And Blood Institute or the National Institutes of Health.

We thank Zahid Latif, Yang Xuan, Yimin Shen for their assistance with the MR protocols, and Dr. Jaladhar Neelavalli and Saifeng Liu for their help on susceptibility mapping.

References

1. Korbas M, Blechinger SR, Krone PH, Pickering IJ, George GN. Localizing organomercury uptake and accumulation in zebrafish larvae at the tissue and cellular level. PNAS. 2008; 105(34):12108–12. [PubMed: 18719123]
2. Gao Y, Liu N, Chen C, Luo Y, Li Y, Zhang Z, et al. Mapping technique for biodistribution of elements in a model organism, Caenorhabditis elegans, after exposure to copper nanoparticles with microbeam synchrotron radiation X-ray fluorescence. J Anal At Spectrom. 2008; 23:1121–4.
3. Samber BD, Evens R, Schamphelaere KD, Silversmit G, Masschaele B, Schoonjans T, et al. A combination of synchrotron and laboratory X-ray techniques for studying tissue-specific trace level metal distributions in Daphnia magna. J Anal At Spectrom. 2008; 23:829–39.
4. Korbas M, O'Donoghue JL, Watson GE, Pickering IJ, Singh SP, Myers GJ, et al. The chemical nature of mercury in human brain following poisoning or environmental exposure. ACS Chem Neurosci. 2010; 1(12):810–8. [PubMed: 22826746]
5. Popescu, BFGh, George, MJ., Bergmann, U., Garachtchenko, AV., Kelly, ME., McCrea, RPE., et al. Mapping metals in Parkinson's and normal brain using rapid scanning X-ray fluorescence. Phys Med Biol. 2009; 54(3):651–63. [PubMed: 19131671]
6. Popescu, BFGh, Robinson, CA., Rajput, A., Rajput, AH., Harder, SL., Nichol, H. Iron, copper, and zinc distribution of the cerebellum. Cerebellum. 2009; 8(2):74–9. [PubMed: 19139969]
7. Popescu, BFGh, Nichol, H. Mapping brain metals to evaluate therapies for neurodegenerative disease. CNS Neurosci Ther. 2011; 17(4):356–68.
8. Leskovjan AC, Kretlow A, Lanzirotti A, Barrea R, Vogt S, Miller LM. Increased brain iron coincides with early plaque formation in a mouse model of Alzheimer's disease. Neuroimage. 2010; 55:32–8. [PubMed: 21126592]
9. Hopp K, Popescu BFGh, McCrea RPE, Harder SL, Robinson CA, Haacke EM, et al. Brain iron detected by SWI high pass filtered phase calibrated with synchrotron X-ray fluorescence. J Magn Reson Imaging. 2010; 31(6):1346–54. [PubMed: 20512886]
10. Habib CA, Zheng W, Haacke EM, Webb S, Nichol H. Visualizing Iron Deposition in Multiple Sclerosis Cadaver Brains American Institute of Physics MASR Conference Proceedings. 2010; 1266:78–83.
11. Antharam V, Collingwood JF, Bullivant J-P, Davidson MR, Chandra S, Mikhaylova A, et al. High field magnetic resonance microscopy of the human hippocampus in Alzheimer's disease: Quantitative imaging and correlation with iron. Neuroimage. 2012; 59:1249–60. [PubMed: 21867761]
12. Chua JY, Tymchak Z, Zheng W, Nichol H, Kelly M, Guzma R. High resolution rapid scanning X-ray fluorescence imaging to track SPIO labeled neural stem cells in an experimental stroke model. Stroke. 2011:e298. [Los Angeles, USA].
13. MacLellan CL, Silasi G, Auriat AM, Colbourne F. Rodent models of intracerebral hemorrhage. Stroke. 2010; 41:S95–8. [PubMed: 20876518]
14. Haacke EM, Cheng NY, House MJ, Liu Q, Neelavalli J, Ogg RJ, et al. Imaging iron stores in the brain using magnetic resonance imaging. Magnetic Resonance Imaging. 2005; 23(1):1–25. [PubMed: 15733784]
15. Schenck JF, Zimmerman EA. High-field magnetic resonance imaging of brain iron: birth of a biomarker? NMR in Biomed. 2004; 17:433–45.
16. Schenck JF. Health and physiological effects of human exposure to whole-body four-tesla magnetic fields during MRI. Ann NY Acad Sci. 1992; 649:285–301. [PubMed: 1580500]
17. Schenck JF. Review article: role of magnetic susceptibility in MRI. Medical Physics. 1996; 23(6): 815–50. [PubMed: 8798169]

18. Duyn JH, van Gelderen P, Li TQ, de Zwart JA, Koretsky AP, Fukunaga M, et al. MRI high-field of brain cortical substructure based on signal phase. Proc Natl Acad Sci USA. 2007; 104(28):11796–801. [PubMed: 17586684]
19. Fukunaga M, Li TQ, van Gelderen P, de Zwart JA, Shmueli K, Yao B, et al. Layer-specific variation of iron content in cerebral cortex as a source of MRI contrast. Proc Natl Acad Sci USA. 2010; 107(8):3834–9. [PubMed: 20133720]
20. Hammond KE, Lupo JM, Xu D, Metcalf M, Kelley DAC, Pelletier D, et al. Development of a robust method for generating 7. 0 T multichannel phase images of the brain with application to normal volunteers and patients with neurological diseases. Neuroimage. 2008; 39(4):1682–92. [PubMed: 18096412]
21. Haacke EM, Xu Y, Cheng YC, Reichenbach JR. Susceptibility weighted imaging (SWI). Magn Reson Med. 2004; 52(3):612–8. [PubMed: 15334582]
22. Lee J, Hirano Y, Fukunaga M, Silva AC, Duyn JH. On the contribution of deoxy-hemoglobin to MRI gray–white matter phase contrast at high field. Neuroimage. 2010; 49(1):193–8. [PubMed: 19619663]
23. Marques JP, Maddage R, Mlynarik V, Gruetter R. On the origin of the MR image phase contrast: an in vivo MR microscopy study of the rat brain at 14. 1 T. Neuroimage. 2009; 46:345–52. [PubMed: 19254768]
24. Petridou N, Wharton SJ, Lotfipour A, Gowland P, Bowtell R. Investigating the effect of blood susceptibility on phase contrast in the human brain. Neuroimage. 2010; 50(2):491–8. [PubMed: 20026280]
25. Sedlacik J, Kutschbach C, Rauscher A, Deistung A, Reichenbach JR. Investigation of the influence of carbon dioxide concentrations on cerebral physiology by susceptibility-weighted magnetic resonance imaging (SWI). Neuroimage. 2008; 43(1):36–43. [PubMed: 18678260]
26. Bradley WGJ. MR appearance of hemorrhage in the brain. Radiology. 1993; 189(1):15–26. [PubMed: 8372185]
27. House MJ, Pierre TGS, Kowdley KV, Montine T, Connor J, Beard J, et al. Correlation of proton transverse relaxation rates (R2) with iron concentrations in postmortem brain tissue vrom Alzheimer's disease patients. Magn Reson Med. 2007; 57:172–80. [PubMed: 17191232]
28. Wharton S, Bowtell R. Whole-brain susceptibility mapping at high field: a comparison of multiple- and single-orientation methods. Neuroimage. 2010; 53:515–25. [PubMed: 20615474]
29. Haacke EM, Tang J, Neelavalli J, Cheng YCN. Susceptibility mapping as a means to visualize veins and quantify oxygen saturation. J Magn Reson Imaging. 2010; 32:663–76. [PubMed: 20815065]
30. Marques JP, Bowtell R. Application of Fourier-based method for rapid calculation of field inhomogeneity due to spatial variation of magnetic susceptibility. Concepts Magn Reson B (Magn Reson Eng). 2005; 25:65–78.
31. Liu T, Spincemaille P, de Rochefort L, Kressler B, Wang Y. Calculation of susceptibility through multiple orientation sampling (COSMOS): a method for conditioning the inverse problem from measured magnetic field map to susceptibility source image in MRI. Magn Reson Med. 2009; 61:196–204. [PubMed: 19097205]
32. Kressler B, de Rochefort L, Liu T, Spincemaille P, Jiang Q, Wang Y. Nonlinear regularization for per voxel estimation of magnetic susceptibility distributions from MRI field maps. IEEE Trans Med Imaging. 2010; 29:273–81. [PubMed: 19502123]
33. Li W, Wu B, Liu C. Quantitative susceptibility mapping of human brain reflects spatial variation in tissue composition. Neuroimage. 2011; 55(4):1645–56. [PubMed: 21224002]
34. de Rochefort L, Liu T, Kressler B, Liu J, Spincemaille P, Lebon V, et al. Quantitative susceptibility map reconstruction from MR phase data using Bayesian regularization: validation and application to brain imaging. Magn Reson Med. 2010; 63:194–206. [PubMed: 19953507]
35. Schweser F, Deistung A, Lehr BW, Reichenbach JR. Quantitative imaging of intrinsic magnetic tissue properties using MRI signal phase: An approach to in vivo brain iron metabolism? Neuroimage. 2011; 54:2789–807. [PubMed: 21040794]

36. Shmueli K, de Zwart JA, van Gelderen P, Li TQ, Dodd SJ, Duyn JH. Magnetic susceptibility mapping of brain tissue in vivo using MRI phase data. Magn Reson Med. 2009; 62:1510–22. [PubMed: 19859937]
37. Yao B, Li TQ, Gelderen PV, Shmueli K, de Zwart JA, Duyn JH. Susceptibility contrast in high field MRI of human brain as a function of tissue iron content. Neuroimage. 2009; 44(4):1259–66. [PubMed: 19027861]
38. Cheng YCN, Neelavalli J, Haacke EM. Limitations of calculating field distributions and magnetic susceptibilities in MRI using a Fourier based method. Phys Med Biol. 2009; 54(5):1169–89. [PubMed: 19182322]
39. Langkammer C, Krebs N, Goessler W, Scheurer E, Ebner F, Yen K, et al. Quantitative MR imaging of brain iron: a postmortem validation study. Radiology. 2010; 257:455–62. [PubMed: 20843991]
40. Langkammer C, Krebs N, Goessler W, Scheurer E, Yen K, Fazekas F, et al. Susceptibility induced gray–white matter MRI contrast in the human brain. Neuroimage. 2012; 59:1413–9. [PubMed: 21893208]
41. Hackett MJ, McQuillan JA, El-Assaad F, Aitken JB, Levina A, Cohen DD, et al. Chemical alterations to murine brain tissue induced by formalin fixation: implications for biospectroscopic imaging and mapping studies of disease pathogenesis. Analyst. 2011; 14:2941–52.
42. Stark, DD., Bradley, WG. Magnetic Resonance Imaging. 3. Mosby, CV., editor. Vol. 3. 1999.
43. Zheng, W., Haacke, EM., Liu, S., Neelavalli, J., Nichol, H. Quantification of susceptibility mapping with synchrotron X-ray fluorescence iron mapping. Montreal, Canada: ISMRM; 2011.
44. Kloska SP, Wintermark M, Engelhorn T, Fiebach JB. Acute stroke magnetic resonance imaging: current status and future perspective. Neuroradiology. 2010; 52:189–201. [PubMed: 19967531]
45. Brown JJ, Peck WW, Gerber KH, Higgins CB, Strich G, Slutsky RA. Nuclear magnetic resonance analysis of acute and chronic myocardial infarction in dogs: alterations in spin–lattice relaxation times. American Heart Journal. 1984; 108(5):1292–7. [PubMed: 6496288]
46. Scholz TD, Martins JB, Skorton DJ. NMR relaxation times in acute myocardial infarction: relative influence of changes in tissue water and fat content. Magn Reson Med. 1992; 23(1):89–95. [PubMed: 1734185]
47. Smith EE, Rosand J, Greenberg SM. Imaging of hemorrhagic stroke. Magn Reson Imaging Clin N Am. 2006; 14(2):127–40. [PubMed: 16873007]
48. Messori A, Polonara G, Mabiglia C, Salvolini U. Is haemosiderin visible indefinitely on gradient-echo MRI following traumatic intracerebral haemorrhage? Neuroradiology. 2003; 45:881–6. [PubMed: 14579110]
49. Duckett S, Galle P, Escourolle R, Poirier J, Hauw J-J. Presence of zinc, aluminum, magnesium in striopalledodentate (SPD) calcifications (Fahr's disease): electron probe study. Acta Neuropathologica. 1977; 38(1):7–10. [PubMed: 857589]
50. Auriat AM, Silasi G, Wei Z, Paquette R, Paterson P, Nichol H, et al. Ferric iron chelation lowers brain iron levels after intracerebral hemorrhage in rats but does not improve outcome. Exp Neurol. 2012; 234(1):136–43. [PubMed: 22226595]

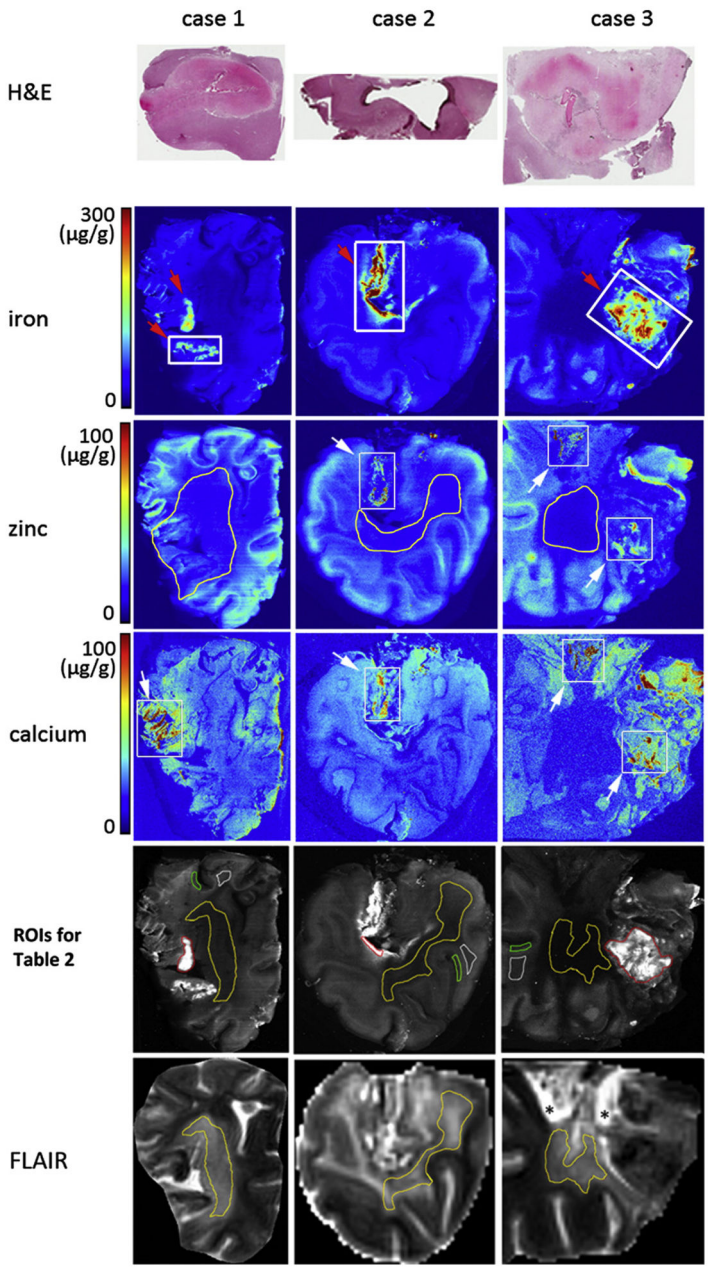

Fig. 1.

Rows 2–4 are XRF iron, zinc and calcium maps of cases 1–3 sections. Row 1 is the histology of the section closest to the hemorrhage area demarcated by the thick white rectangles drawn on the XRF iron maps. White arrow in zinc maps shows where zinc colocalizes with calcium. White arrow in calcium maps shows regions with a high concentration of calcium (>100 μg/g wet weight). The hemorrhagic lesions are pointed by red arrows in Fe maps. ROIs of hemorrhage (red), normal WM (white), GM (green) and chronic ischemic WM infarct (yellow) for the measurements in Table 2 are outlined in gray-scaled Fe map (Row 5). Row 6, the FLAIR images manually rotated (in SPIN) to be co-

registered with XRF maps. Outlined regions in Row 6 indicate where the ROIs of WM infarct (Row 5) are registered from. Asterisk indicates gelatin.

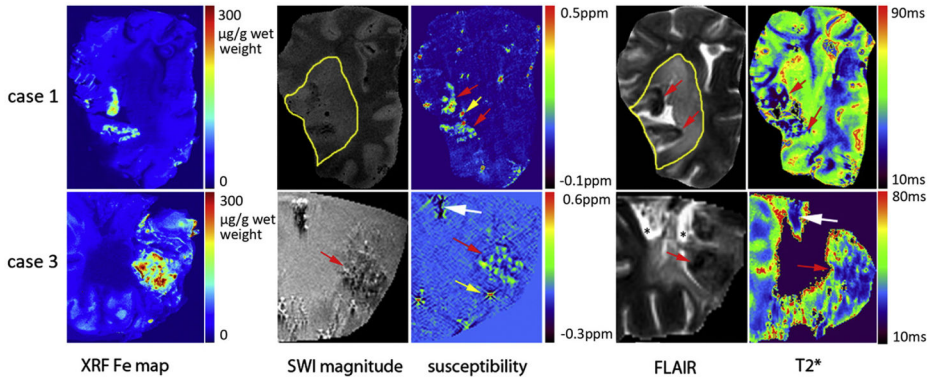

Fig. 2.

Correlation between XRF iron maps and MR imaging [SWI magnitude images (TE=18.5 ms), susceptibility maps (TE=8.2 ms), FLAIR and T2* maps] for Cases 1 and 3. The white arrows indicate possible calcification. The red arrows show the high iron regions corresponding to iron in XRF. The intense spots in the susceptibility map are artifacts caused by air bubbles (yellow arrows). Ischemic lesions are outlined in FLAIR images and SWI magnitude. Signal void in T2* maps means either it was not possible to fit T2* because of poor SNR in those locations or the T2* values in these voxels are larger than 300 ms due to the partial volume effect, partial gelatin and partial tissue in a voxel. SRS-XRF iron maps colocalize well with the higher susceptibility in susceptibility map.

Table 1

Demographic and clinical information on autopsy brain samples

Case	Age of stroke lesions	Age/sex	Clinical and neuropathology	Code
1	Recent ischemia with hemorrhagic transformation	81/F	The external view and the coronal sections show a large irregular area of hemorrhage, tissue discoloration, and cavitation throughout most of the lateral 50% of the right middle cerebral artery territory. There is no other apparent softening, discoloration, hemorrhage, mass, or lesion. Sections of the lesion show near complete neuronal loss with associated early gliosis, early macrophage infiltration, endothelial proliferation, and focal hemorrhage. Other features included: chronic obstructive pulmonary disease, mild to moderate atherosclerosis, evidence of recent ischemia, degenerative disc disease and one hip replacement.	3968
2	Ischemia 7 years prior to death along with cerebral infarction and necrosis	71/M	The section of occipital lobe shows multiple superficial areas of necrosis, lymphocytic infiltration, scattered marcophages, and a few examples of hemosiderin. The white matter shows rarefaction and increased number of corpora amylacea. Also present were: cerebral infarction of intermediate age (i.e., 7-year-old infarct), cerebral, hypoxia, recent and mild; with a 7 year history of stroke, chronic obstructive pulmonary disease, atrial fibrillation and hypertension.	3065
3	Ischemia 3 years prior to death	80/F	Ischemic stroke, 3 years prior to death along with hypertension, hypothyroidism and cancer of the breast and bowel. Right cortex and basal ganglia show history of cerebral infarction. Cerebrovascular accident with left mouth-droop. Small vessel infarction	1714

Table 2

Average elemental concentrations in some hemorrhage and infarct regions (μg/g wet weight)

	Case	Hemorrhage	Normal cortical gray matter	Chronic Ischemic lesion	Normal White matter
Fe	1	126±39	32±6	19±6*	35±5
	2	323±133	42±7	32±10*	47±5
	3	177±75	45±12	13±11*	45±10
Zn	1	18±3 (*n*=5605)*	22±3 (*n*=1010)	17±2 (*n*=42336)*	23±3 (*n*=1727)
	2	11±2 (*n*=552)*	20±3 (*n*=427)	17±3 (*n*=13860)*	23±3 (*n*=565)
	3	23±10 (*n*=13618)*	29±6 (*n*=713)	11±5 (*n*=12950)*	28±6 (*n*=2543)

Note: The data is mean±standard deviation. *n* is the number of pixels, same for the measurements in Fe maps. Asterisk indicates significance ($P<.05$) compared with normal white matter.